ELSEVIER

Solid State Ionics 131 (2000) 51–60

SOLID STATE IONICS

www.elsevier.com/locate/ssi

Nanoscale variation in electric potential at oxide bicrystal and polycrystal interfaces

Bryan D. Huey, Dawn A. Bonnell*

The University of Pennsylvania, Department of Materials Science, Philadelphia, PA 19104, USA

Received 1 September 1999; accepted 1 December 1999

Abstract

Scanning surface potential microscopy (SSPM), has been used to measure spatial variations in grain boundary properties in $SrTiO_3$ and ZnO. Experimental measurements of a Fe-doped $SrTiO_3$ $\Sigma 3$ bicrystal are compared to finite element calculations to quantify the effects of tip geometry and sample-tip separation. Experimental and numerical treatments include realistic tip interactions and lateral inhomogeneity in sample properties. A procedure for extracting actual interface potentials from separation dependence is proposed. Both the sign and magnitude of the grain boundary potential barrier measured with SSPM agree with macroscopic measurements. For experimentally available tips, the effect of tip geometry was found not to contribute to uncertainty. In application to polycrystalline materials, the voltage dependence of individual interface properties has been determined in micropatterned, ZnO-based, polycrystalline varistor devices.

Keywords: Atomic force microscopy; Surface potential; SSPM; Interface potential; Oxide

1. Introduction

To support continued miniaturization and hybridization of oxide electronic devices, a fundamental understanding of interfacial effects at the nanometer scale is necessary. It is at this spatial scale that potential barriers exist due to charge trapped at interfaces, facilitated by segregation of dopants and impurities [1] as well as the presence of thin amorphous layers [2,3]. Such scales are experimentally difficult to access, and relevant property measurements at oxide interfaces have only been achieved using either transmission electron microscopy (TEM) or probe-based measurements. For example, scanning tunneling microscopy (STM) has been used to detect variations in conductivity at polycrystalline ZnO grain boundaries [4], and to measure Schottky barrier formation at the interfaces between TiO_2 and metal clusters [5]. Electrostatic force detection based on atomic force microscopy (AFM) at in situ biased Nb-doped TiO_2 polycrystals observed the voltage dependence of grain boundary potential barriers [6]. Potential variations were quantified using scanning surface potential microscopy (SSPM), in an investigation of ZnO varistor materials also with in situ applied biases [7]. This technique was applied by Nabhan et al. [8] to directly observe potential barriers in acceptor p-type poly-

*Corresponding author. Tel.: +1-215-898-6231; fax: +1-215-573-2128.

E-mail address: bonell@soll.lrsm.upenn.edu (D.A. Bonnell)

0167-2738/00/$ – see front matter
PII: S0167-2738(00)00621-4

crystalline silicon. Vandervorst et al. [9] applied a scanning probe tip as a contact voltage probe to detect potential variations in CMOS transistors. For the particular case of $SrTiO_3$ bicrystal interfaces Maier et al. [10,11] have investigated tilt and twist acceptor-doped $SrTiO_3$ bicrystal interfaces at temperatures above 500°C using macroscopic impedance measurements and in situ electrocoloration. Dravid et al. [12] employed holographic phase contrast in TEM to estimate the charge and potential barrier associated with bicrystal grain boundaries, and to observe the disappearance of the barrier with the application of large external biases [13]. However, difficulties in interpretation and sample preparation for in situ TEM studies suggest that probe-based techniques may be better suited for the investigation of samples of interest to the device fabrication community.

Since the scanning techniques of surface potential measurement are new and in situ measurements have only been accomplished recently, careful consideration of tip–sample interactions and resolution limits based on model experiments is required. This paper first compares surface potential measurements of bicrystal interfaces by SSPM with numerical calculations. The spatial variation of the interface potential barrier of well characterized $SrTiO_3$ bicrystals provides the model system. Finally, individual grain boundaries of polycrystalline ZnO-based commercial varistors were investigated under in situ applied fields, allowing determination of the voltage dependence of grain boundary electronic properties and demonstrating the general application of the approach.

2. Experimental details

A bicrystal presents an ideal geometry with which to investigate interactions between a tip and a true sample surface. A 70.6° pure tilt $\Sigma 3$ grain boundary along the {111} plane in acceptor-doped $SrTiO_3$ (4.8×10^{18} Fe atoms/cm^3) was fabricated using the Verneuil method [14]. Macroscopic conductivity and capacitance measurements at elevated temperatures (500–1000°C) yielded average values for the grain boundary potential barrier and depletion width of 300 mV and 400 nm, respectively (the activated carrier concentration is 2.6×10^{17} charges/cm^3) [15]. The ideal atomic structure of the grain boundary core was measured with high resolution transmission electron microscopy for similar samples (1.3×10^{19} Fe atoms/cm^3 $\Sigma 3$ {111} bicrystals); the interface was found to consist of Sr and O atoms at the boundary plane with perfect mirror symmetry [16]. The bicrystal used herein was polished with diamond impregnated films down to 0.05 μm grit size. To apply local lateral electrostatic fields to the interface, a grid of 400 nm thick, 100 μm diameter Al contacts separated by 350 μm gaps was electron beam evaporated through a shadow mask onto the surface of the bicrystal.

Individual grain boundaries in commercial ZnO-based polycrystalline varistors [17] were isolated using microlithography. Contacts were deposited on these samples using standard lift-off metallization described in detail elsewhere [7]. The measurement is considered in situ because micropatterning allows external lateral biases to be applied at individual grain boundaries during SSPM. Biases were applied with a function generator (Wavetek model 20), and current was monitored with a multimeter (Keithly model 175) connected in series with the sample.

The configuration of local electrostatic potential variation near an interface is described as follows. A two dimensional defect such as a grain boundary can trap charge, and in an oxide the consequence to local field variation extends over a large range due to the magnitude of the dielectric constants. Using traditional semiconductor models, a grain boundary interface charge can be treated as a delta function, with an oppositely charged depletion region extending into the adjacent grains so that charge is conserved. Fig. 1(a), left, depicts a negative grain boundary charge (infinitesimally thin) as well as a positive depletion region (in extinction and using the abrupt junction approximation). Solving Poisson's equation for this charge density distribution yields the equilibrium energy band diagram indicated in Fig. 1(b), left, for a n-type semiconductor. In the event that a positive bias (V) is applied to the right grain while the left grain is grounded, the depletion region lengthens or shortens for the 'reverse' and 'forward' biased grains, respectively. The interface charge can also increase, if empty interface states above the Fermi level are available. The charge distribution for

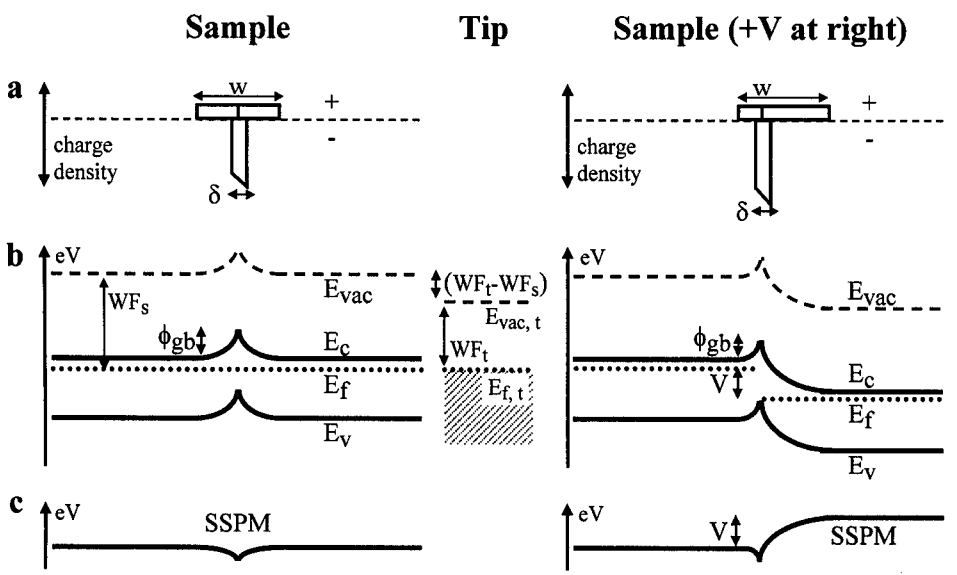

Fig. 1. The relationship between (a) charge density, (b) energy band diagram, and (c) measured surface potential for a grounded npn junction or polycrystalline grain boundary in thermal equilibrium with the SSPM tip (center). The left and right sides, respectively, depict the model without and with an external bias (V) applied to the right side. Parameters include: w = depletion width; δ = thickness of p region ($\rightarrow 0$); ϕ_{gb} = potential barrier height; WF_s and WF_t = work function of sample and tip, respectively; and E_{vac}, E_c, E_f, and E_v = vacuum level, conduction band, Fermi level, and valence bands.

this biased case is shown at the far right of Fig. 1(a), while the right of Fig. 1(b) indicates the modified band diagram for an external applied bias. The potential barrier broadens, becomes asymmetric, and decreases in magnitude.

To measure the voltage dependence of potential barriers, SSPM was employed. SSPM is based on the century old concept of a Kelvin probe [18] or null force probe [19–22]. Sensitivity to the surface potential of a sample is achieved by nulling the capacitive force acting on a biased Permalloy coated AFM tip oscillating above a surface. Using standard intermittent contact AFM, the grounded tip first acquires a trace of the surface topography in the vicinity of a grain boundary intersecting a surface. The tip then retraces the topographic profile, separated from the surface 50–100 nm, thereby maintaining a constant tip-sample separation. During the second scan, a variable DC bias (V_{Null}) is applied to the tip (V_{Tip}) as well as a fixed frequency AC bias ($V_{AC} \cdot \sin(\omega t)$). This leads to a potential difference (ΔV) between tip and an arbitrarily biased sample (V_{Sample}) that includes DC and AC components, where the work functions of tip and sample (WF) are considered:

$$\begin{aligned}\Delta V &= V_{Tip} - V_{Sample} \\ &= (V_{Null} - V_{Sample} - (WF_{Tip} - WF_{Sample})) \\ &\quad + V_{AC}\sin(\omega t) = V_{DC} + V_{AC}\sin(\omega t)\end{aligned}$$

The capacitive force exerted on the tip above the surface is then proportional to the square of ΔV, resulting in three distinct force components (DC, ω, and 2ω), where z is the separation between tip and specimen and C_{Eff} is the total effective capacitance including the tip apex, tip edges, and cantilever surface:

$$\begin{aligned}F &= \frac{1}{2}\cdot\frac{\partial C_{Eff}}{\partial z} \\ &\quad \cdot\left[\left(V_{DC}^2 + \frac{1}{2}V_{AC}^2\right) - \frac{1}{2}V_{AC}^2\cos(2\omega t)\right. \\ &\quad \left. + 2V_{DC}V_{AC}\sin(\omega t)\right]\end{aligned}$$

The force component acting on the tip (and causing

it to oscillate) at ω will be eliminated (null) when the adjustable tip bias and the sample surface potential are equal ($V_{DC}=0$), offset by the differences in work function:

$$V_{Null} = V_{Sample} + (WF_{Tip} - WF_{Sample})$$

In this manner, the surface potential at any position of the surface is determined by recording the adjustable tip bias (V_{Null}) that nulls the tip oscillation at ω. Fig. 1(c) depicts the anticipated SSPM profiles for the grounded and biased cases of the grain boundary with negative interface charge considered in Fig. 1(a) and (b). As can be seen, SSPM yields the surface potential, which is the mirror image of the energy band diagram, offset by the tip–sample work function difference. It is important to note that the tip and sample apparent work functions can be affected by surface adsorption. However, assuming that this effect is constant with lateral position, the measured surface potential is offset by a constant and spatial variations are valid.

This simplified description of SSPM does not take into account capacitive interactions between the biased tip and a *heterogeneous* surface potential in the sample. Fig. 2 depicts this case, including six distinct regions of differing surface potential. Following Henning et al. [5], the equation that describes the force acting on the tip at ω for n distinct surface regions is thus revised (where $C_{Eff,i}$, $V_{S,i}$, and $WF_{S,i}$ represent the ith components of capacitance, surface potential, and work function for the surface region 'i,' respectively, and $V_{Null,Het}$ is the measured surface potential by the SSPM tip) [23]

$$F_{Tip,\omega} = \frac{\partial C_{Eff}}{\partial z} V_{DC} V_{AC} = V_{AC} \sum_{i=1}^{n} \frac{\partial C_{Eff,i}}{\partial z} V_{DC,i}$$

$$= V_{AC} \sum_{i=1}^{n} \frac{\partial C_{Eff,i}}{\partial z} [V_{Null,Het} - V_{S,i} - (WF_{Tip} - WF_{S,i})]$$

Solving for $F=0$, the analytical solution for the SSPM measured surface potential of a heterogeneous sample ($V_{Null,Het}$) is:

$$V_{Null,Het} = \frac{\sum_{i=1}^{n} \frac{\partial C_{Eff,i}}{\partial z} [V_{S,i} + (WF_{Tip} - WF_{S,i})]}{\sum_{i=1}^{n} \frac{\partial C_{Eff,i}}{\partial z}}$$

These relations are used in the comparison of experimental results and numerical calculations.

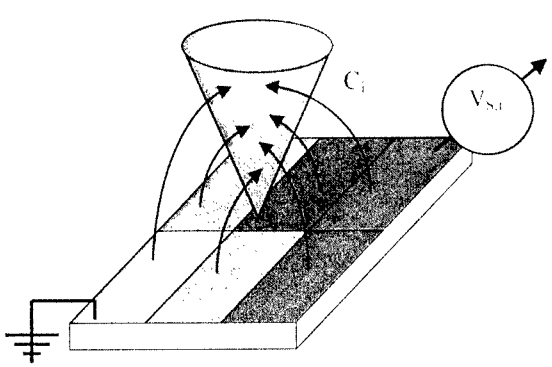

Fig. 2. Schematic diagram of how a heterogeneous potential distribution on a sample surface contributes to the capacitance measured by a tip. Regions directly below the tip affect a smaller tip area than do surrounding regions, resulting in a non-linear interaction.

3. Results and discussion

The topographic structure of the $\Sigma 3$ $SrTiO_3$ grain boundary is shown in Fig. 3(a), where only polishing damage is visible. Fig. 3(b) reveals a variation in the surface potential measured with a tip height of 80 nm that takes the form of a ridge of raised surface potential. The contrast variation is more visible in Fig. 3(c). The average height of this feature is 25 mV (95% confidence is ± 9 mV), and the depletion width is 2770 ± 40 nm. It is noteworthy that the grain boundary is not visible in the topography; the position was confirmed ex situ by electron backscattering (EBSP) in a scanning electron microscope (SEM) [24]. Note that the feature clearly varies with position, ranging from 11 to 39 mV in height and 2.150–3.520 μm in width (in excess of the experimental energy noise of 5 mV). Furthermore, the 'apparent' interface potential and depletion width depend on the height at which the image was obtained. Table 1 summarizes 'apparent' properties at several heights.

The presence of increased surface potential at the grain boundary position can only result from a depression in the corresponding band diagram, the

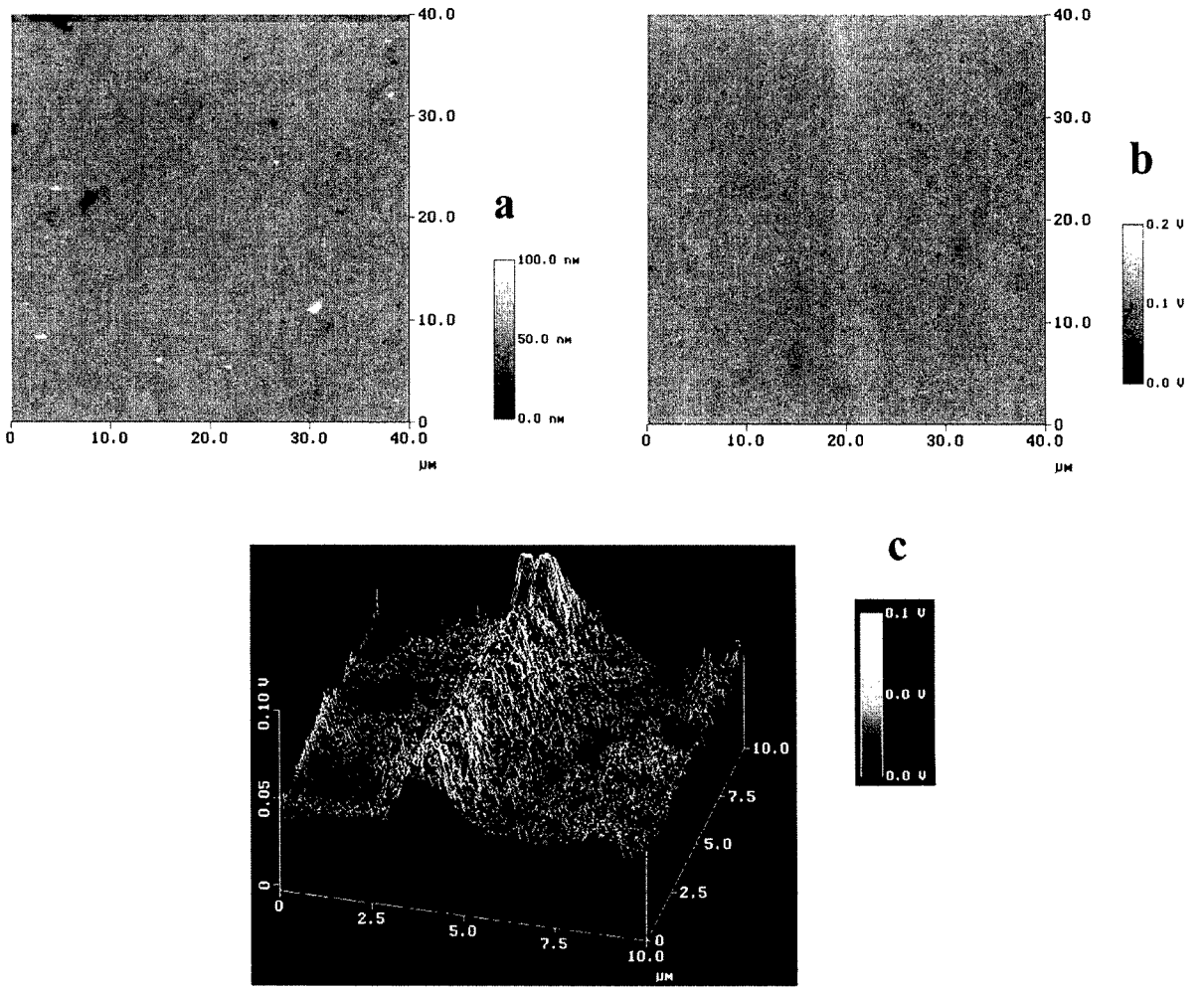

Fig. 3. Topographic structure (a) and surface potential in plan view (b) and 3-D rendering (c) of a $SrTiO_3$ Σ3 grain boundary.

Table 1
Dependence of apparent properties on tip height

Apparent property	$z=60$ nm	$z=80$ nm	$z=100$ nm
Interface potential (mV)	46±5	25±9	17±2
Depletion width (nm)	1770±170	2770±40	3240±30

inverse of Fig. 1(c), as expected for an acceptor-doped material. A potential trough indicative of positive interface charge impedes current flow, because positive charge carriers dominate conduction for the bicrystal in contrast to the n-type varistors. The 'apparent' interface potential is of the same sign but is approximately one order of magnitude lower than the macroscopically derived potential barrier properties [10]. This discrepancy may be due to interactions between the surface and the entire tip, mediation of the SSPM results by the presence of surface charge, or attenuation of electrostatic fields away from the surface complicated by the heterogeneous potential distribution at the grain boundary. In an effort to quantify these effects, two-dimensional finite element calculations [25] discretely solving Poisson's equation for the experimental tip/sample geometry are compared.

Fig. 4(a) and (b) depict the model used in the simulation, including a tip with a 50 nm radius of curvature, a tip length of 12.5 μm, a tip half angle of

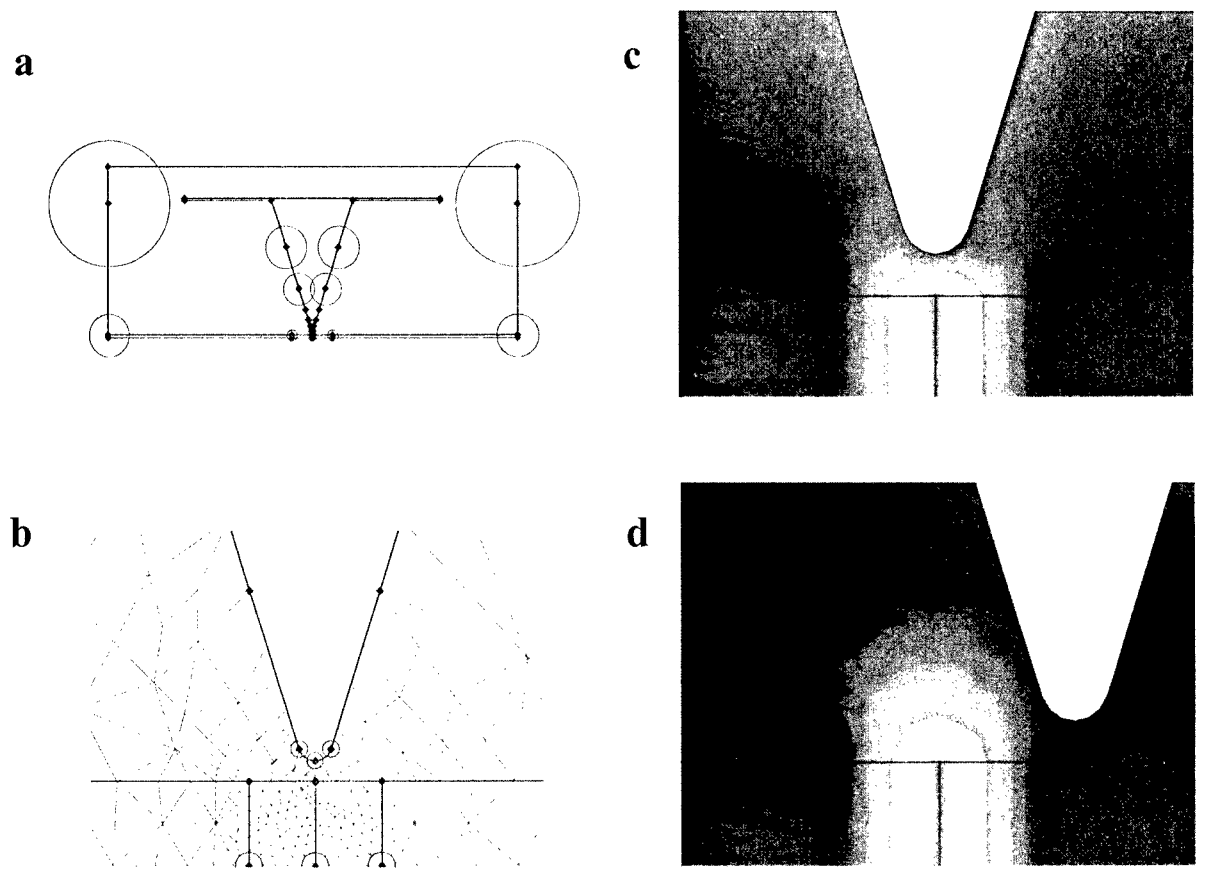

Fig. 4. Two dimensional finite element calculations of a charged grain boundary intersecting a surface. The model includes tip (length = 12.5 μm, half angle = 17.5°) and cantilever width = 25 μm. (a) The details in the tip region (b) show the interface which has a charge of $+1\times10^{13}$ e/cm^2, and adjacent depletion regions with -2.6×10^{17} e/cm^3. Solutions for the electric potential with the tip over the interface (c) and displaced laterally (d) are compared.

17.5°, a cantilever width of 25 μm, a tip–sample separation of 60 nm, and a grain boundary with the macroscopic potential barrier oriented perpendicular to the surface. Boundary conditions include a positive interface charge of $+1.0\times10^{13}$ charges/cm^2 for the centered grain boundary, a potential barrier of 300 mV, and symmetric, negatively charged depletion regions extending 200 nm into each of the adjacent grains with an ionized acceptor concentration of -2.6×10^{17} charges/cm^3. The number of nodes at which Poisson's equation is discretely solved is 485, where at least 25 nodes are always present between the tip apex and the sample (the simulation mesh is indicated in Fig. 4(b), a close-up of Fig. 4(a)). Fig. 4(c) shows the simulation in the vicinity of the tip lifted directly above the grain boundary, in which the contrast represents the potential distribution ranging between 0 and 300 mV (darkest to lightest). A parabolic potential barrier exists at the interface as anticipated. The tip experiences a net null force in the simulation following the procedure of Jacobs et al. [26]. By repeating calculations with the tip at successively larger lateral displacements from the grain boundary, as exemplified in Fig. 4(d), a potential barrier profile simulating the SSPM experiment is obtained. Fig. 5 depicts the calculations for the experimental tip geometry, as well as a SSPM measured surface potential profile extracted from a potential image acquired 60 nm above the surface. Note that the calculated potential maximum agrees

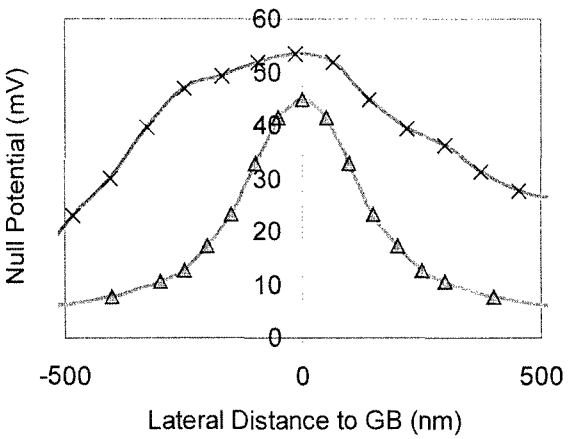

Fig. 5. Comparison of experimental (cross hatches) and calculated (triangles) potential profiles at 60 nm above the surface. The average experimentally measured potential maximum was 46±5 mV.

with the average measured value, 46 mV, although the particular profile compared in the figure is in the upper range of the experimental distribution.

Of course electric fields decay with distance from the surface so the measured valued depends on the height at which it was obtained. To extract the actual value at the surface, the distance dependence of results from the numerical calculations is parameterized, thus accounting for the inhomogeneous surface potential and realistic tip dimensions. The ideal relation, i.e. that from the calculations, can be described as:

$$\Phi_z = \Phi_0 \exp[Bz^C]$$

where Φ_z is the potential measured at some height z, Φ_0 is the potential at the interface, B and C are constants that characterize the complex sample–tip interaction, equal -0.47 ± 0.01 and 0.345 ± 0.005, respectively. Using this functional form to determine the interface potential from the measurements yields 260 ± 10 mV, in good agreement with macroscopic measurements.

The 'apparent' depletion depth measured with SSPM is larger than expected from macroscopic transport measurements. Tip geometry is an obvious and well known factor in spatial resolution degradation in scanning probe microscopies. To quantify this effect, numerical calculations with models similar to that in Fig. 4 were done for the most 'ideal' shapes available as conducting tips [27]. These calculations showed a negligible dependence of the potential barrier height on tip geometry at heights in the range of 60–100 nm; differences of 10–20% in apparent feature width might be determined for tips with radii of curvature between 25 nm up to an upper limit of 200 nm. A procedure for extracting the actual value from the measurements has not yet been developed.

The remaining differences between properties determined from macroscopic transport studies and local probe measurements may be related to sample conditions. It is known that oxide surfaces adsorb atmospheric molecules that alter the surface charge [28]. The presence of surface charge might dampen or heighten lateral potential variations. Preliminary simulations accounting for surface charge and associated surface band bending suggest this effect is negligible. It is also possible that the interface intersects the surface at an angle that deviates from 90°. Relative misorientation determined by EBS is less than ±5° and would not account for significant variations in depletion width. Finally, the bicrystal grain boundary may not be as perfect macroscopically as suggested by TEM. Amorphous interfacial films, facets, and pores are likely to exist along the boundary. This possibility is supported by recent near field optical studies on similar bicrystals and thin films [29].

With this insight, polycrystalline materials can be quantified from several perspectives. Fig. 6(a) and (b) compare the topography and surface potential of the ZnO varistor when leads just to the left and right of the imaged region are grounded. Again, a grain boundary is not apparent in the topographic structure. Two regions of depressed surface potential exist in Fig. 6(b) (≈70 mV), resulting from the presence of second phases with a larger apparent work function than that of the surrounding grains (including the mediation of the sample work function by surface adsorbates). These regions have been confirmed to be Bi and Ti rich second phases by energy dispersive spectroscopy in SEM [7]. Fig. 6(c) and (d) depict the surface potential distribution when a bias of ±1 V is externally applied to the left contact, respectively, causing current flow through the var-

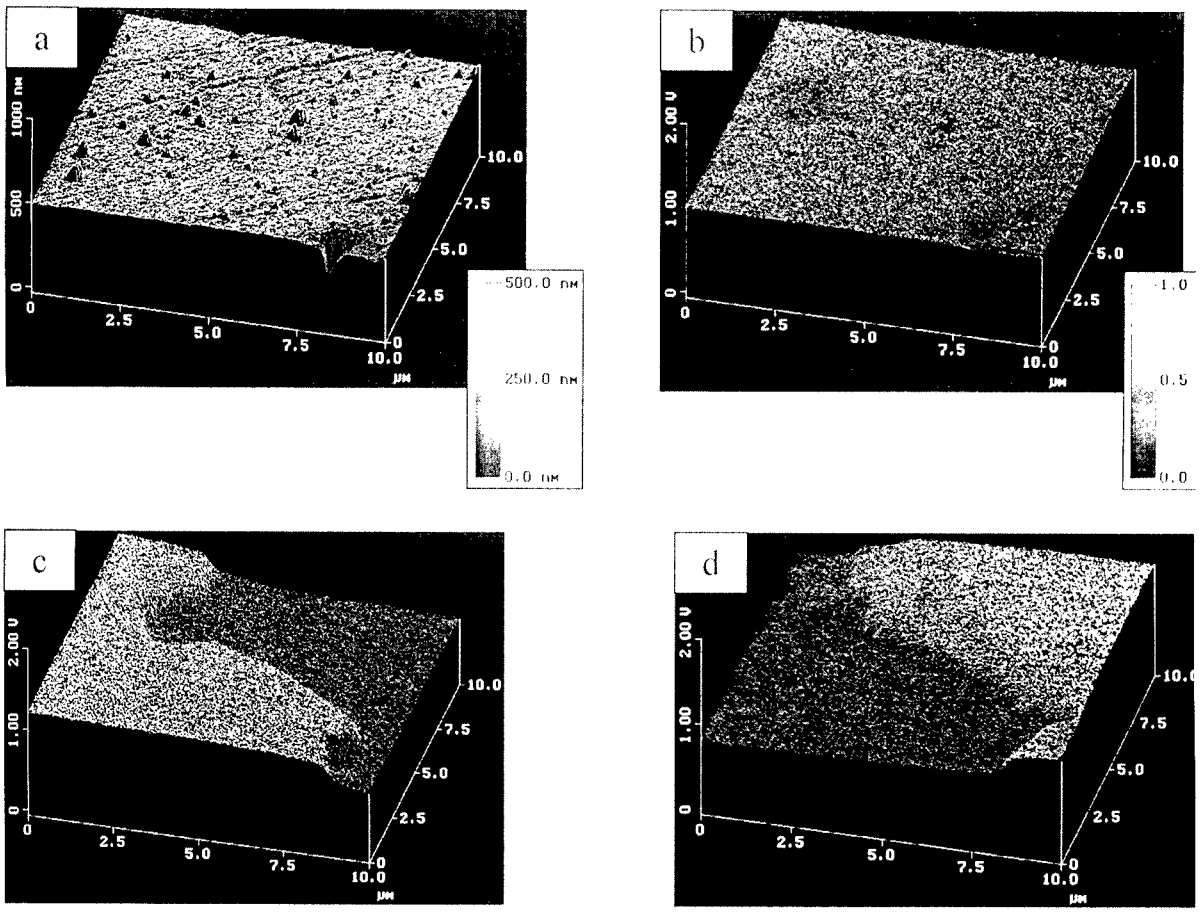

Fig. 6. Topographic structure (a) and surface potential of unbiased region of a polycrystalline ZnO surface. Surface potential variation at a grain boundary with laterally applied (c) forward and (d) reverse bias (±1.00 V applied approximately 30 μm to the left and right).

istor during this in situ SSPM experiment. The sharp, irregular contrast step in the center of these surface potential images represents a highly resistive feature, resulting from the presence of a potential barrier containing grain boundary. The height of the potential step is approximately 190 mV, although it varies as a function of position (220–160 mV from top to bottom of the 10 μm grain boundary). The potential step also inverts when the polarity of the external bias is reversed, as expected, except at the 2nd phases where the electrically active interface switches from one side to the other of the impurity region. Reanalyzing Fig. 6(b), an average step of 7 mV exists along the entire grain boundary correlating to the difference in relative effective work functions of the adjacent grains.

Extracting surface potential profiles at a given position for a series of external biases, and knowing the current flowing through the device during the in situ SSPM measurements, the voltage dependence of the potential barrier can be determined. Current is assumed to flow by thermionic emission over the potential barrier (E_F refers to the Fermi energy with respect to the conduction band minimum; k is Boltzman's constant; T is room temperature; I/Area is the measured current density flowing through the

leads during the in situ experiment (the cross sectional area is taken from the microfabricated contact dimensions); and V_{app} is the bias dropping at the grain boundary measured directly from SSPM profiles):

$$\phi_{gb}(V) = -E_F - kT \cdot \ln\left[\frac{1}{AT^2}\cdot\frac{I/\text{Area}}{1-\exp\left(-\frac{V_{app}}{kT}\right)}\right]$$

Fig. 7 presents the voltage dependence of the individual potential barrier from Fig. 6 and compares results from the local and macroscopic measurements. The two curves for the local properties represent upper and lower bounds for the actual potential barrier directly beneath the tip. Specifically, the lower bound is obtained by assuming all measured current flows through (over) the potential barrier directly beneath the tip. The upper bound is determined assuming that a purely resistive current path exists somewhere between the contacts in parallel with the studied potential barrier. This constant shunting resistor is defined by the resistance between the leads at zero applied bias. For either limiting case, the local properties of the single boundary differ substantially from the macroscopic, average response.

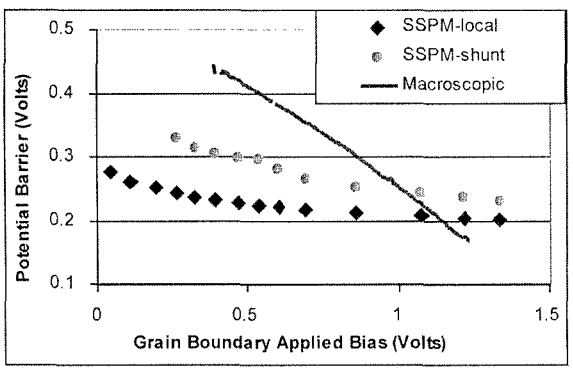

Fig. 7. SSPM derived local voltage dependence of individual grain boundary potential barrier in Fig. 6 compared to the macroscopic properties that average over hundreds of grain boundaries. The two curves for the local data represent the upper and lower limits due to assumptions regarding the current path.

4. Conclusion

A correlation of scanning probe-based measurements of surface potential and actual local properties has been made for the case of a charged interface intersecting a surface. The potential barrier of an acceptor-doped, $SrTiO_3$ $\Sigma 3$ bicrystal grain boundary is found to correspond to a positively charged interface and a negative depletion charge. There is an intrinsic experimental problem with measurement at the surface so the actual properties must be extracted from measurements above the surface. Analytical solutions of simple geometries would not provide the correct relation between the experiment and properties because the tip–sample interactions are complex due to tip geometry and sample inhomogeneity. This model system allowed characterization of realistic tip–sample interactions and lateral sample inhomogeneity by two dimensional finite element analysis. A relation that was determined numerically was applied to experimental measurements to extract actual local properties. Extending SSPM to study grain boundaries of micropatterned polycrystalline ZnO varistors, the voltage dependence of individual interfaces has been measured in situ. There is a significant difference between the macroscopically derived barrier response and the voltage dependence of the individual grain boundary.

Acknowledgements

We are grateful to Prof. J. Maier, Max-Planck-Institute fur Festkorperforschung, Stuttgart, Germany for providing the bicrystal and for helpful discussion. This work was supported by the Department of Energy, Office of Basic Energy Sciences under grant # DEFG02-90ER-45428. The support of the Laboratory for Research on the Structure of Matter is acknowledged for use of the Scanning Probe Facility and Electron Microscopy. The assistance of V. Dominko with microfabrication and of S. Kalinin with mathematical analysis is appreciated.

References

[1] T.K. Gupta, Microstructural engineering through donor and acceptor doping in the grain and grain-boundary of a polycrystalline semiconducting ceramic, J. Mater. Res. 7 (12) (1992) 3280.

[2] E. Olsson, G.L. Dunlop, R. Osterlund, Development of interfacial microstructure during cooling of a ZnO varistor material, J. Appl. Phys. 66 (v. 15) (1989) 5072–5077.

[3] H.F. Wang, Y.M. Chiang, Thermodynamic stability of intergranular amorphous films in bismuth-doped zinc oxide, J. Am. Ceram. Soc. 81 (1) (1998) 89.

[4] D. Bonnell, I. Solomon, Measurement of space charge adjacent to oxide grain boundaries by tunneling spectroscopy, Ultramicroscopy 42–44 (1992) 788–792.

[5] D.L. Carroll, M. Wagner, M. Ruhle, D.A. Bonnell, Schottky barrier formation at nanoscale metal-oxide interfaces, Phys. Rev. B 55 (15) (1997) 9792–9799.

[6] D.A. Bonnell, B.D. Huey, D.L. Carroll, In situ measurement of electric fields at individual grain boundaries in TiO_2, Solid State Ionics (1995).

[7] B.D. Huey, D. Lisjak, D.A. Bonnell, Nanometer scale variations in interface potential by scanning probe microscopy, J. Am. Ceram. Soc. (1999) accepted.

[8] W. Nabhan, B. Equer, A. Broniatowski, G. DeRosny, A high-resolution scanning Kelvin probe microscope for contact potential measurements on the 100 nm scale, Rev. Sci. Instr. 68 (8) (1997) 3108.

[9] T. Trenkler, P. De Wolf, W. Vandervorst, Nanopotentiometry: local potential measurements in complementary metal-oxide-semiconductor transistors using atomic force microscopy, J. Vac. Sci. Technol. V 16 (1) (1998) 367–371.

[10] I. Denk, J. Claus, J. Maier, Electrochemical investigations of $SrTiO_3$ boundaries, J. Electrochem. Soc. 144 (10) (1997) 3526–3536.

[11] I. Denk, F. Noll, J. Maier, In situ profiles of oxygen diffusion in $SrTiO_3$: Bulk behavior and boundary effects, J. Am. Ceram. Soc. 80 (2) (1997) 279–285.

[12] V. Ravikumar, R.P. Rodrigues, V.P. Dravid, An investigation of acceptor-doped grain boundaries in $SrTiO_3$, J. Phys. D: Appl. Phys. 29 (1996) 1799–1806.

[13] K.D. Johnson, V. Dravid, Grain boundary barrier breakdown in niobium donor-doped strontium titanate using in situ electron holography, Appl. Phys. Lett. 74 (4) (1999) 621–623.

[14] Frank & Schulte Gmbh, Essen, Germany.

[15] M. Leonhardt, Personal Communication, 1998.

[16] O. Kienzle, F. Ernst, Effect of shear stress on the atomistic structure of a grain boundary in strontium titanate, J. Am. Ceram. Soc. 80 (7) (1997) 1639–1644.

[17] Harris Semiconductor, type V24RA22.

[18] J. Janata, 100th anniversary of the Kelvin probe. AVSNewsletter, 1997(May/June): p. 4–5.

[19] M. Nonnenmacher, M.P. O'Boyle, H.K. Wickramasinghe, Kelvin probe force microscopy, Appl. Phys. Lett. 58 (25) (1991) 2921–2923.

[20] M. Nonnenmacher, M. Oboyle, H.K. Wickramasinghe, Surface investigations with a Kelvin probe force microscope, Ultramicroscopy 42 (1992) 268.

[21] H.O. Jacobs, H.F. Knapp, S. Muller, A. Stemmer, Surface potential mapping: a qualitative material contrast in SPM, Ultramicroscopy 69 (1997) 39–49.

[22] J.M.R. Weaver, D.W. Abraham, High resolution AFM potentiometry, J. Vac. Sci. Technol. B 9 (3) (1991) 1559–1561.

[23] A.K. Henning, T. Hochwitz, Scanning probe microscopy for 2-D semiconductor dopant profiling and device failure analysis, Mater. Sci. Eng. B – Solid State M 42 (1–3) (1996) 88.

[24] EBSP patterns collected in JEOL 6400 SEM using a Merlin LTC216-F40E low light camera, a custom Camera Designs Ltd. CCU-1852C camera control unit, and a Hamamatsu Argus 10 image processor.

[25] QuickField v. 4.1, Tera Analysis.

[26] H.O. Jacobs, P. Leuchtmann, O.J. Homan, A. Stemmer, Resolution and contrast in Kelvin probe force microscopy, J. Appl. Phys. D 84 (3) (1998) 1168–1173.

[27] G.D. Skidmore, E.D. Dahlberg, Improved spatial resolution in magnetic force microscopy, Appl. Phys. Lett. 71 (22) (1997) 3293–3295.

[28] D.A. Bonnell, Atomic structure of transition metal oxide surfaces from scanning tunneling microscopy, Progr. Surf. Sci. 57 (1998) 187–252.

[29] B.D. Huey, D.A. Bonnell, to be published.

[30] J.W.P. Hsu, E.B. McDaniel, R.A. Rao, C.B. Eom, Mater. Res. Soc. 474 (1997) 91–98.